ISSN 0020-4412, Instruments and Experimental Techniques, 2010, Vol. 53, No. 3, pp. 334–349. © Pleiades Publishing, Ltd., 2010.
Original Russian Text © V.M. Aulchenko, O.V. Evdokov, I.L. Zhogin, V.V. Zhulanov, E.R. Pruuel, B.P. Tolochko, K.A. Ten, L.I. Shekhtman, 2010, published in Pribory i Tekhnika Eksperimenta, 2010, No. 3, pp. 20–35.

NUCLEAR EXPERIMENTAL TECHNIQUES

A Detector for Imaging of Explosions on a Synchrotron Radiation Beam

V. M. Aulchenko[a], O. V. Evdokov[b], I. L. Zhogin[b], V. V. Zhulanov[a], E. R. Pruuel[c], B. P. Tolochko[b], K. A. Ten[c], and L. I. Shekhtman[a]

[a] *Budker Institute of Nuclear Physics, Siberian Division, Russian Academy of Sciences, pr. Akademika Lavrent'eva 11, Novosibirsk, 630090 Russia*
e-mail: L.I.Shekhtman@inp.nsk.su
[b] *Institute of Solid-State Chemistry and Mechanochemistry, Siberian Division, Russian Academy of Sciences, ul. Kutateladze 18, Novosibirsk, 630128 Russia*
[c] *Lavrent'ev Institute of Hydrodynamics, Siberian Division, Russian Academy of Sciences, pr. Akademika Lavrent'eva 15, Novosibirsk, 630090 Russia*

Received September 17, 2009

Abstract—Synchrotron radiation (SR) offers a unique chance to study the structure of a substance in fast processes. Since SR is emitted by electron bunches in a storage ring, the SR burst corresponding to a single bunch may be very short. Should a detector capable of detecting SR from a single bunch without mixing signals from different bunches be available, it is possible to obtain information on changes in the state of the material in a sample under investigation with a very high time resolution. A detector for imaging of explosions on an SR beam—DIMEX—has been developed by the Budker Institute of Nuclear Physics (Siberian Division of the Russian Academy of Sciences, Novosibirsk). This detector is a high-pressure ionization chamber with a strip readout at a pitch of 0.1 mm. The electron component of primary ionization is collected within 50 ns, which is substantially shorter than the orbital period of a bunch in the VEPP-3 storage ring (250 ns). The DIMEX is filled with a Xe–CO_2 mixture (3 : 1) at an absolute pressure of 7 atm. The spatial resolution of the detector is ~210 μm, and its efficiency for radiation with an energy of 20 keV is ≥50%. The dynamic range of the detector is ~100, which allows one to measure the signal with an accuracy of ~1%. In this case, the maximum flux of X-ray photons, at which the DIMEX operates in a linear region, is ~10^{10} photons/(channel s). Today, the detector has been used in experiments aimed at studying evolution of the density in detonation waves and processes of nanoparticle production at the VEPP-3 storage ring by employing the small-angle X-ray scattering technique.

DOI: 10.1134/S0020441210030036

INTRODUCTION

Synchrotron radiation (SR) is a unique tool for studying the structure of a substance. The time dependence of the SR flux is governed by the length and quantity of electron bunches in a storage ring. For example, in the VEPP-3 storage ring at the Budker Institute of Nuclear Physics (BINP) of the Siberian Branch of the Russian Academy of Sciences, the bunch length is ~30 cm and the orbital period is 250 ns; therefore, SR is emitted in a single-bunch mode by bursts with a duration of ~1 ns and a period of 250 ns. The integral SR flux is very high. In the VEPP-3, the SR flux density from the wiggler with a field of 2 T at a distance of 20 m from the source is >10^{12} photons/(mm^2 s) at an electron energy of 2 GeV and a current of 100 mA with allowance for the absorption in the 2-mm-thick exit Be window. In this case, the mean SR energy is close to 20 keV. These beam parameters help obtain the photon flux density of >10^5 photons/mm^2 from one bunch, which provides a means for X-ray imaging, i.e., for measuring the radiation absorption coefficient in a sample located on the beam path (i.e., its X-ray density) with an accuracy of about a percent and a spatial resolution of ~0.1 mm.

To implement this technique, one must use a detector capable of measuring the distribution of the photon flux density with a high efficiency (~50%) and a high spatial resolution (~100 μm). Incidentally, this detector must be able to measure the signal from one bunch before the signal arrives from the next bunch and to store the signal from a sequence of several tens of bunches to allow investigation of changes in the sample over time. These detector parameters will also allow it to be used to measure the small-angle X-ray scattering (SAXS) from a single bunch and record changes in the SAXS with time. The SAXS is governed by fluctuations of the electron density in the sample and factually provides a means for recording formation and evolution of nanoparticles in a sample under investigation.

In this paper, we describe the DIMEX detector developed by the BINP for imaging of explosives on the SR beam [1–3]. The DIMEX measures SR from

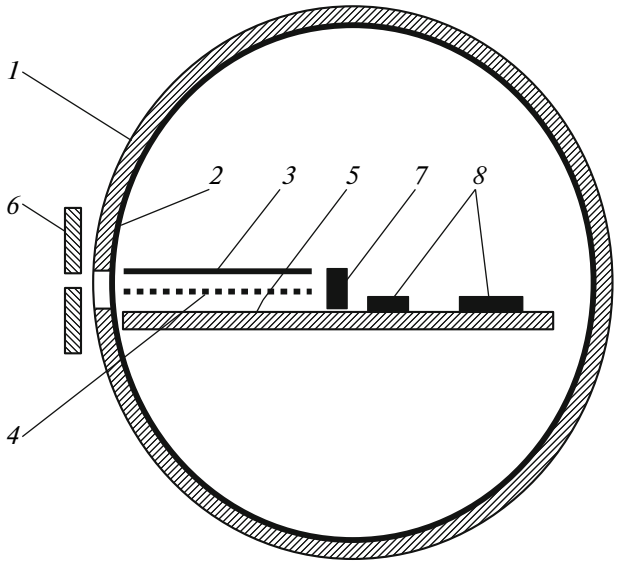

Fig. 1. Schematic diagram of the DIMEX detector: (*1*) aluminum casing with the entrance window, (*2*) 1-mm-thick coal-plastic insert, (*3*) drift electrode, (*4*) GEM, (*5*) strip structure, (*6*) entrance aperture, (*7*) radiation shielding of the electronics, and (*8*) integrator chips and other electronic components.

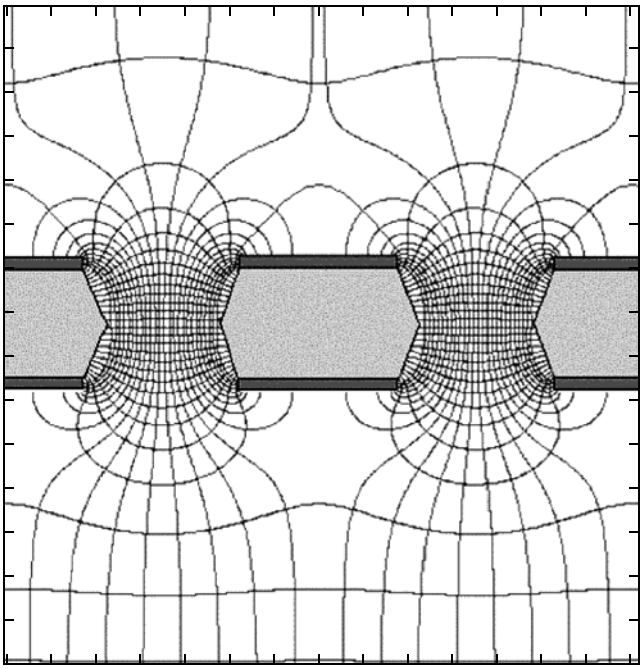

Fig. 2. Cross sectional view of the GEM structure with a pattern of the electric field lines.

individual bunches and does not mix the signals from consecutive bunches. It is able to record 32 images, each of which is an array of 256 to 512 coordinate channels (detector modifications differ in the number of channels). The DIMEX is currently being used to conduct experiments on the SR beamline at the VEPP-3 storage ring. In this paper, we also discuss the feasibility of using the DIMEX at the VEPP-4M storage ring with higher energy SR beams.

DESIGN AND OPERATING PROCEDURE OF THE DETECTOR

Detector Design

The DIMEX detector is a high-pressure ionization chamber with a strip readout. The strips are located with a pitch of 0.1 mm. The SR beam collimated in a vertical direction enters the sensitive volume of the detector through a 1-mm-thick entrance window made of coal plastic or beryllium (different materials of the entrance window were used in detector modifications). Depending on the type of the experiment, the beam has a vertical dimension of 0.1–1.0 mm and a horizontal dimension of up to 14 mm. The SR beam penetrated into the gas volume between two parallel electrodes (Fig. 1): a high-voltage drift electrode, to which a negative potential is applied, and a strip readout plane, the strips of which are parallel to the beam.

The detector is filled with a $Xe–CO_2$ mixture (3 : 1) at an absolute pressure of 7 atm; the depth of the sensitive volume downstream of the beam is 30 mm. SR photons are absorbed in the working gas, producing primary ionization. Primary ionization electrons drift toward the readout strip structure, while positive ions move toward the drift electrode. A gaseous electron multiplier (GEM) is located on the path of the drifting electrons at a distance of 1.5 mm from the strip structure; it shields the readout structure from the positive ion field. The GEM is a polymer film (polyimide) 50 μm thick with double-sided metallized coating and through holes ∅~80 μm in diameter that form a regular hexagonal structure with a pitch of ~140 μm [4, 5] (Fig. 2). When a voltage is applied between the metallized GEM plates, electrons in the gas drift through the holes. Depending on the electric field strength outside and inside the holes, electrons can either increase in number due to collision ionization during their drift through the GEM holes, or decrease in number through partial neutralization upon absorption at the top or bottom GEM plates. In the DIMEX detector, the GEM operates in a mode such that gas amplification does not occur and, on the contrary, electrons decrease in number as they drift through the GEM.

After penetration through the GEM, some electrons continue drifting toward the strip structure. In this case, a charge is induced on strips; it arrives at the inputs of low-noise integrators connected to each individual strip. The field of positive ions is fully shielded by the GEM plates and does not affect the charge induced on the strips of the readout structure.

It should be noted that positive ions drift ~1000 times slower than electrons and create a region with a high density of the space charge in the gap between the

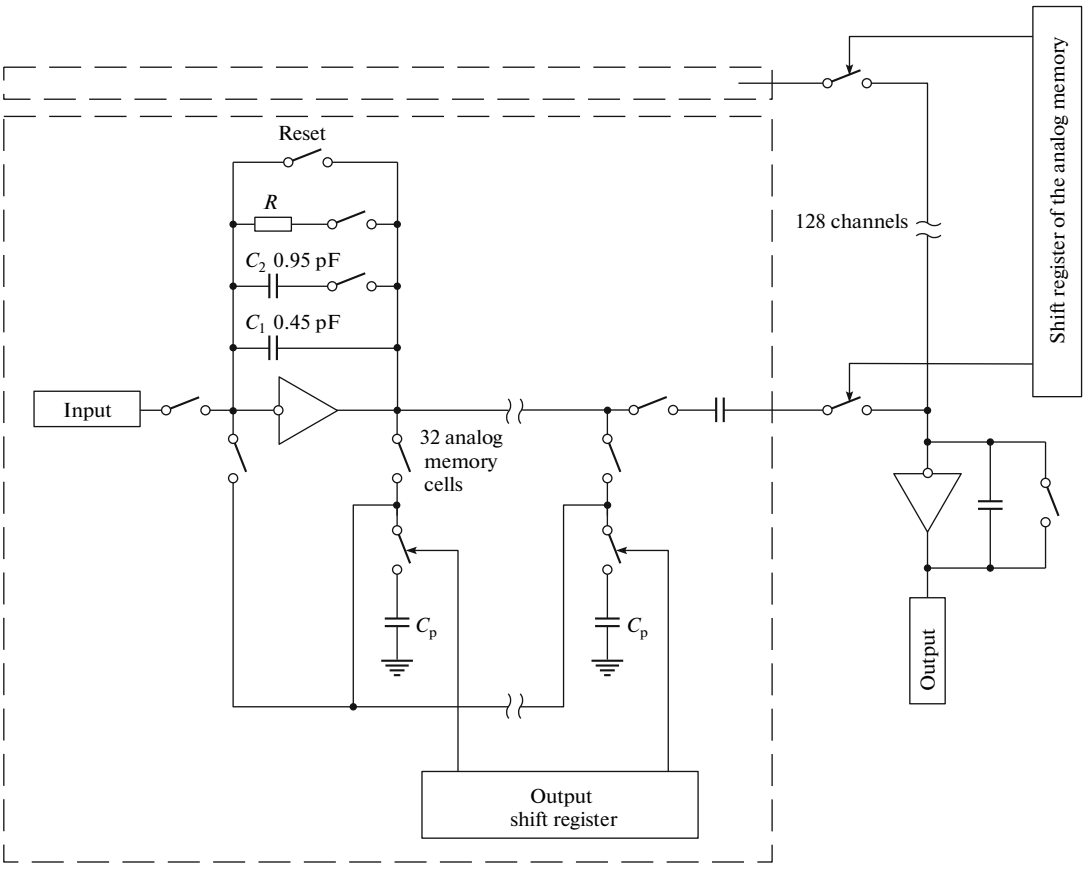

Fig. 3. Diagram of the APC128 chip.

SR beam plane and the drift electrode. At a sufficiently high SR flux density, this space charge may shield the field so that both the drift velocity of electrons and the GEM transparency change.

Detector Electronics and Operating Procedure

Since fast detection of a signal from each electron bunch is the primary task of the detector, the electronic system selected is such that the signal is recorded in the analog memory during an experiment, being digitized and read out after the end of measurements. Each strip of the detector's readout structure is connected to the input pad of the APC128 integrators chip [6]. The APC128 is an unpacked chip containing 128 channels, each of which consists of a low-noise integrator at the input and 32 analog memory cells. In addition, the chip contains an output analog multiplexer, through which all channels can be sequentially read. (The maximum frequency for reading and scanning the analog memory is 10 MHz.) The APC128 integrator has two different feedback capacitors for changing its sensitivity. The equivalent integrator noise referring to the input does not exceed 2000 electrons. The circuit diagram of the APC128 is shown in Fig. 3.

After the power is turned on and the program controlling operation of the detector electronics is loaded, the measuring cycle is started. Each analog memory cell is connected to the integrator output, the integrator stores the charge arriving from the strip of the readout structure, the memory cell is thereafter disconnected, and the integrator feedback capacitor is cleared. Afterward, the next analog memory cell is connected to the integrator input, and so on. In this case, memory cells are filled cyclically, with rewriting of the earliest value. This process independently proceeds in all channels of all chips. As a result, at each instant of time, the analog memory contains information about the signal stored over 32 time intervals preceding the current instant of time.

The time structure of the measuring cycle is determined by the *Clock* signal, which is derived from the *Phase* signal of the accelerator that has a frequency of 4 MHz. The *Clock* signal has a frequency of 40 MHz in the first detector modification and 160 MHz in the last version. By the *Start* signal, one can stop the process of writing into memory cells or continue the cycle for a fixed number of time intervals. This provides flexibility for selection of the method for the synchronizing operation of the detector and the device that starts an experiment (e.g., a generator of the detonation wave in

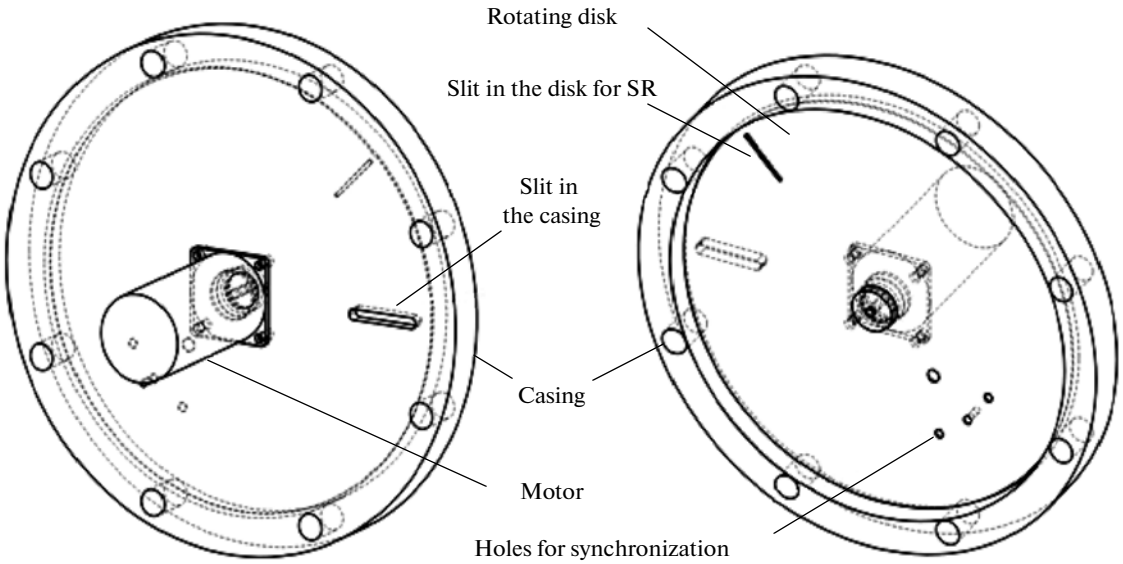

Fig. 4. Structural diagram of the fast-acting shutter.

a sample), since the *Start* signal can be produced either before the interesting event or after it.

A fast-acting shutter that opens the SR flux only for the time of an experiment is used to reduce the space charge of positive ions being accumulated in the drift gap. The shutter is a disk with a narrow slit, rotating with a period of 18 ms (Fig. 4). The shutter opens for 60 μs, which is sufficient for carrying out an experiment. The time between two open-shutter phases is enough for positive ions to reach the drift electrode. For the disk position to be determined, there are three closely spaced holes in it. A light guide is located opposite these holes on the one side of the disk, and a photodiode is located on the other side. When the disk rotates, a sequence of three pulses is induced in the photodiode. Based on these pulses, the instant when the slit passes through the optoelectronic couple is determined, and the current disk speed is determined from the time interval between two such sequences. The signal from the optoelectronic couple is processed by the control unit and it calculates the time to the next phase of shutter opening. A certain time is subtracted from this value in order to compensate for the delay in generation of the detonation wave and its propagation to the sample region exposed to SR. On the expiry of the calculated time, a command is issued to the generator of pulses for the detonator.

The block diagram of the experimental setup is shown in Fig. 5. The control unit responsible for synchronization of the experiment is the key component of the setup. In the first detector modification, it was a special module made to the CAMAC standard; in the latest modification, the control unit was integrated with the DIMEX detector. The control sequence of commands for carrying out an experiment is launched by an operator from the computer. In this case, the program in the control unit expects for the next sequence of pulses from the fast-acting shutter and produces a command for the generator of pulses for the detonator in view of the generator's response time and the instant when the fast-acting shutter opens. The spread of time between the command for the generator and production of the detonation wave in a sample may exceed 10 μs. Therefore, a wire sensor composed of two parallel wires is used for more precise synchronization of the *Start* signal for the detector. The wires close upon passing of an ionized plasma in the detonation wave. This sensor can also be located so that it operates after the interesting event and does not disturb the detonation wave. In this case, the detector stops the write cycle immediately after the arrival of the *Start* signal, storing information on the interesting event in the analog memory. After stopping the write cycle, the program operating in the FPGA of the DIMEX detector starts the read cycle. In response to this command, the charge is read out of the analog memory of all APC128 channels via an output analog multiplexer, is digitized, and buffered in the memory located on the detector; afterward, all information is transmitted over the Ethernet channel to the computer (Fig. 6). The latest detector modification has 512 channels (four APC128 chips).

Detector Characteristics

The detector must be capable of measuring the distributions of the X-ray photon flux with a high accuracy in the coordinate and the value. In addition, the ability of the DIMEX detector to detect a signal arriving from each flying electron bunch before passage of the next bunch is the most important property of this

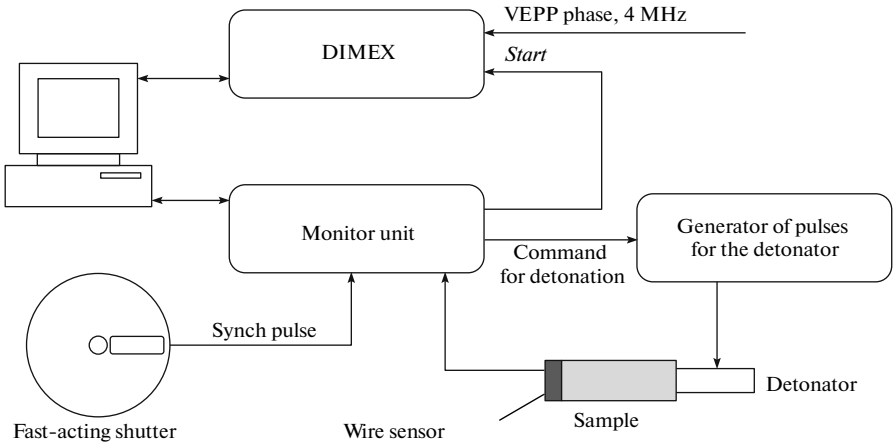

Fig. 5. Block diagram of the experimental setup for the VZRYV station.

detector. Therefore, the spatial resolution, the accuracy in measuring the signal value (the signal-to-noise ratio and the dynamic range), and the time resolution are the most critical detector parameters. Incidentally, since the photon flux from a single bunch is limited, the quantum efficiency (which must be rather high) is an important property of the detector.

Spatial Resolution and Efficiency

The spatial resolution of the detector is determined by the ranges of secondary particles produced upon absorption of an X-ray photon in the working gas (photoelectrons, Auger electrons, and fluorescent photons), as well as by diffusion of electrons during their drift toward the strip structure. The photoelectron ranges depend, in turn, on the energy of incident X-ray photons.

The energy spectrum of SR from the wiggler with a field of 2 T at the entrance into the detector is shown in Fig. 7. The calculation was made using the XOP2.0 code. The figure presents the spectra after passing through a 3-m-thick air layer at the exit from the vacuum channel and after passing through explosive samples 5 and 10 mm thick. It is apparent that, after passing through a 10-mm-thick sample, the most probable energy in the emission spectrum is ~20 keV. The mean energy in this spectrum is also close to 20 keV.

The theoretical dependence of the DIMEX efficiency (i.e., the fraction of the photon flux absorbed in the sensitive region) on the energy of X-ray photons is shown in Fig. 8. The calculation was made using the XOP2.0 code for an expected energy spectrum of SR from a 5-pole wiggler with a field of 1.3 T at the VEPP-4M storage ring at a beam energy of 4 GeV after passing through an explosive sample 20 mm thick. Pure carbon with a density of 1.2 g/cm^3 was taken as the sample material. The thickness of the dead zone behind the entrance window is 3 mm, and the thickness of the sensitive zone is 30 mm. The working gas is a Xe–CO_2 mixture (3 : 1) at a pressure of 7 atm. It is apparent that the fraction of the absorbed flux exceeds 50% in the energy region of 15–30 keV.

The effect of different physical processes and detector parameters on the spatial resolution was determined by simulation using the FLUKA2006.03 software package [7, 8]. FLUKA is a versatile package for Monte Carlo simulation, with which it is possible to simulate particle transport and calculate results of particle interactions with a substance. FLUKA provides a means for performing precise simulations of transport and interactions with a substance for 60 different particles (in particular, photons and electrons) with energies ranging from 1 keV to several thousand TeV.

The simulated distribution of the signal in the detector irradiated by an infinitely narrow photon beam with an energy of 20 keV is shown in Fig. 9. The detector configuration and its materials in this simulation are similar to those used in the calculation of the efficiency (see above). The result of the simulation was obtained ignoring diffusion of electrons during their drift from the gap between the drift electrode and the GEM toward the strip structure. Diffusion of electrons is added by convolution of the obtained distribution with the Gaussian function with a variance determined by the drift length and the diffusion coefficient. The drift length is assumed to be 2.5 mm, and the transverse diffusion coefficient is taken from [9] for the Ar–CO_2 mixture (3 : 1). The square root of the variance for the corresponding Gaussian distribution is 33 μm. The distribution of the signal from the infinitely thin beam in the detector with diffusion allowed for is also shown in Fig. 9. It is apparent that diffusion of electrons makes the main contribution to the spatial resolution.

The measured spatial resolution is shown in Fig. 10. The line spread function of the detector (the image of the infinitely thin beam), measured using the opaque edge method, is also shown in Fig. 10. In this

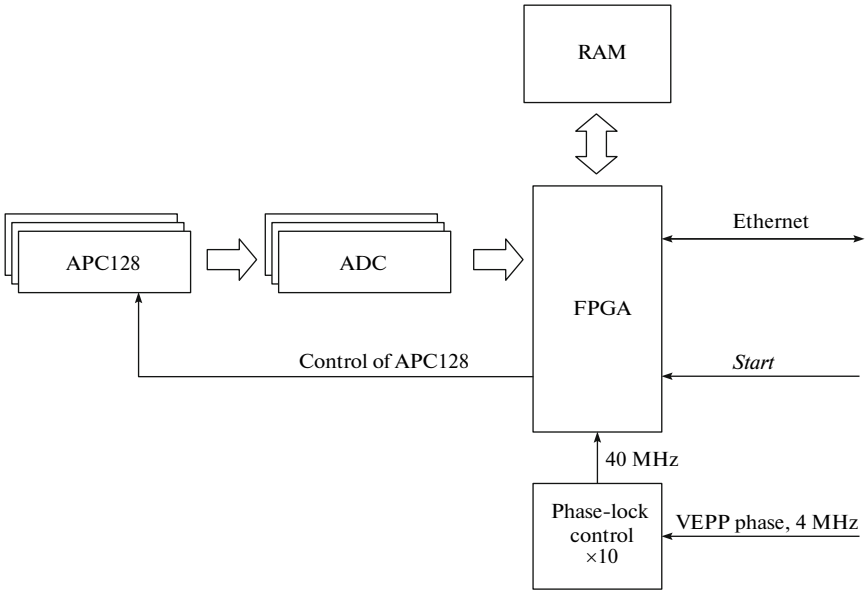

Fig. 6. Block diagram of the DIMEX electronics.

case, an opaque sample with an accurately treated edge is placed in the uniform beam. The image of the edge is thereafter differentiated, and the obtained distribution is the sought line spread function. It is apparent that the full width at half-maximum (FWHM) of the function is 210 μm, which is in good agreement with the result of the simulation with due account of the electron diffusion.

Time Resolution

The time resolution of the DIMEX detector is governed by the time it takes for collection of all electrons drifting through the induction gap. Using the data in [9] for the $Ar–CO_2$ mixture (3 : 1), we can draw a conclusion that the drift velocity is ~5 cm/μs at a field intensity of >1 kV/(cm atm). In this case, the time of the drift through a 1.5-mm gap is 30 ns. The electron collection time is also dependent on the SR beam thickness and the longitudinal diffusion, which is ≤0.1 mm (the FWHM of the distribution). At a maximum SR beam thickness of 1 mm, the collection time of electrons is ≤50 ns.

The bunch period in the VEPP-3 is 250 ns, and the maximum frequency for writing into the analog memory of the APC128 chip is 10 MHz. Therefore, the sole method for testing the time resolution of the detector is to record the SR signal within 125 ns; in this case, the signal must be recorded every second cycle. The ratio of the signals recorded in two sequential cycles is the measure of the time resolution.

The result of such a measurement is shown in Fig. 11, which presents the dependence of the signal on the analog memory cell number. Record in the memory was made within 125 ns; in this case, the charge stored in the feedback capacitor of the APC128 integrators was not reset. Therefore, recording of the signal from the next bunch implies an increase in the signal value, while the absence of a bunch in a measurement cycle corresponds to the absence of a variation in the signal. In Fig. 11, it is apparent that no greater than 5% of the total signal (i.e., the sum of the signals in two sequential cycles) is recorded during a cycle when the bunch is absent. If we assume that the electron flux decreases over time according to the exponential law, $\leq 2.5 \times 10^{-4}$ of the total signal will be recorded in 250 ns. This value corresponds to the mix-

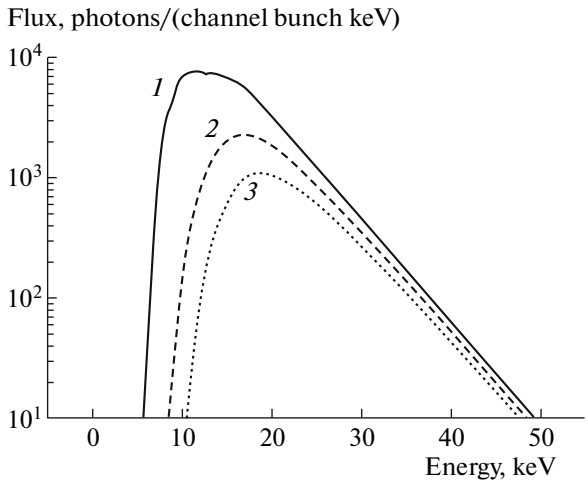

Fig. 7. Energy spectra of SR in the VZRYV station at the VEPP-3: (*1*) spectrum at the exit from the vacuum channel after passing 3 m in air and (*2*, *3*) spectra after passing through EM samples 5 and 10 mm thick, respectively.

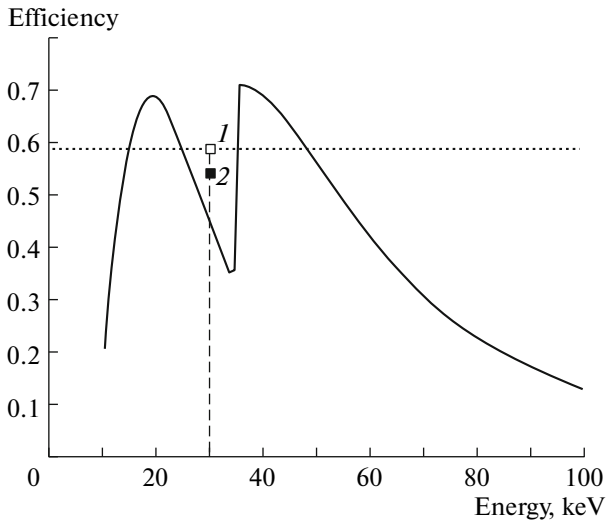

Fig. 8. Energy dependence of the detector quantum efficiency (calculation using the XOP2.0 code): (*1*) results of simulation of the efficiency and (*2*) DQE for a photon beam with the energy distribution corresponding to spectrum *3* (see Fig. 17).

ing coefficient of the signals from two sequential bunches.

Accuracy in Measuring the Signal and the Dynamic Range

The accuracy in measuring the signal is determined both by fluctuations of the detected photon flux and by electronic noise. The dependences of the detector signal and the signal-to-noise ratio (SNR) on the photon flux incident on the detector are shown in Fig. 12. The photon flux was varied by means of Plexiglas (PMMA) filters. The flux calculated using the XOP2.0 code is presented in the graph. The signal is seen to increase in direct proportion to the incident flux over the whole measurement range. The SNR varies as the square root of the signal (the slope of the dependence is twofold smaller on the double logarithmic scale). Therefore, fluctuations of the number of detected photons are the factor determining the signal measurement accuracy, and the best accuracy is attained at a maximum signal.

The limiting signal measurable by the detector is limited by the dynamic range of APC128 integrators. Since integrators are saturated at a certain value of the input signal, the maximum detectable photon flux can be increased by reducing the charge detected from one photon. This effect can be attained by changing the fraction of the electron flux passing through the GEM and by varying the relation between the electric field value in the GEM holes and in the drift and induction gaps [10]. One should bear in mind that further increase in the photon flux absorbed in the drift gap will give rise to another significant effect that restricts the limiting flux—the space charge of positive ions. Positive ions accumulated in the drift gap shield the electric field. A decrease in the electric field leads to a decrease in the drift velocity of electrons, enhancement of their recombination, and, finally, a decrease in the signal. To reduce this effect, one should increase the field in the drift gap and inject a photon beam as close as possible to the drift electrode in order to reduce the density and thickness of the ion layer.

From Fig. 12, it is apparent that, at a maximum signal in the detector, the SNR is close to 100; i.e., it is possible to measure variations in the signal at a level of 1%. Today, we perform further investigations of the possibility of extending the dynamic range and improving the accuracy of measurements using the above technique.

THE USE OF DIMEX IN EXPERIMENTS

Below, we describe two experiments on the SR beam with the use of the DIMEX detector.

Tomography of the Density and the Flow Field of Detonation Products Using SR

Tomographic methods for examining the density of static objects have been developed and successfully used. As applied to dynamically changing objects, they are used with lesser success in gas dynamics and plasma physics for determining the temperature and the density [11] and in pulsed X-ray density radiography [12]. In these tasks, it is nearly always impossible to obtain experimental data from different angles with a high accuracy. Therefore, selection of the error-tolerant reconstruction algorithm capable of efficiently using a priori information on the sample under investigation is of principal importance for high-quality density reconstruction.

The use of the VEPP-3 storage ring as a radiation source (with its high X-ray flux) and the DIMEX as a detector offers a chance to conduct explosion experiments with a nanosecond exposure and a spatial resolution of ~100 μm. The procedure of these experiments was described in [13, 14].

To determine the spatial distribution of the density in detonation products of a cylindrical charge of explosive material (EM) in a particular cross section, the X-ray shadow was sequentially recorded with a 0.5-μs interval between frames (Fig. 13). The amount of material examined with X-rays along the beam was determined from the X-ray flux attenuation using the appropriate calibration.

The method for reconstructing the density by the recorded X-ray shadow from the sample under investigation was developed in the above papers. This method is based on regularization, involves a priori information on the type of the sought function, and provides a means for attaining a high accuracy in reconstructing distribution $\rho(r, z)$. This method was used to recon-

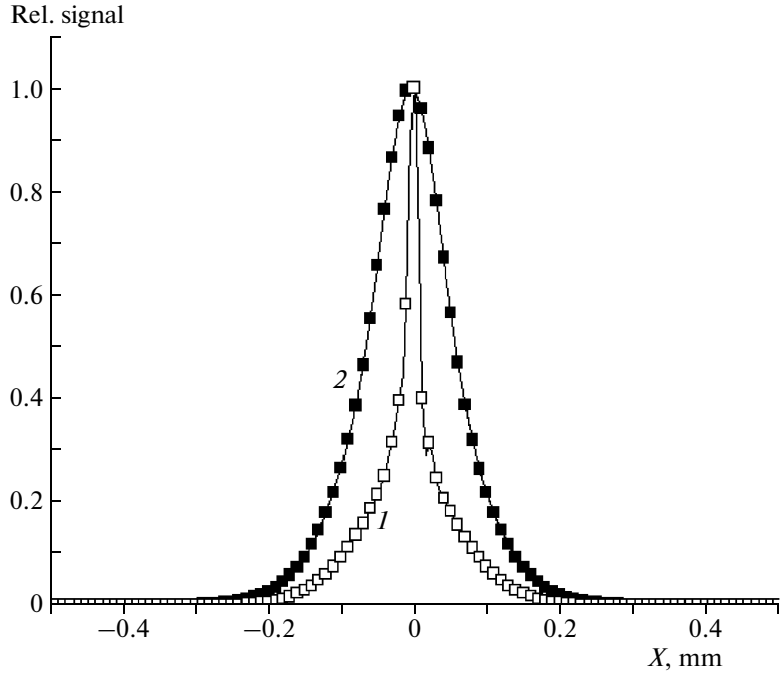

Fig. 9. Charge distribution in the detector under irradiation with an infinitely narrow beam (simulation results). The distributions were obtained (*1*) ignoring diffusion and (*2*) taking into account diffusion of electrons at a photon energy of 20 keV.

struct spatial density distribution $\rho(r, z)$ of expanding TNT explosion products, which is presented in Fig. 14.

Tomographic data for detonation products of pressed charges made from a mixture of trotyl and hexogen (TH 50/50) with an initial density of 1.7 g/cm^3 and detonation speed $D = 7.6$ km/s were presented in [15]. The diameter of the charges was 15 mm, and the distance from the initiated end surface to the cross section in which measurements were taken was 60 mm. A plane wave generator was used for the initiation. Since the process is steady-state, the relationship between time t and spatial coordinate $z = Dt$ is used in data representation.

Knowing density distribution $\rho(r, z)$, we can state a problem of reconstructing the other flow parameters, i.e., the fields of the mass velocity and pressure. To solve it, we can use the system of equations of stationary gas dynamics

$$\mathrm{div}(\rho \mathbf{v}) = 0, \quad (1)$$

$$\mathrm{div}(\rho v \mathbf{v}) + \nabla p = 0. \quad (2)$$

In this case, the energy conservation equation is not used, and the equation for the state of detonation products may be unknown. Such a statement is an untraditional approach to solving gas dynamic equations, and, in general, possible correct statement of the problem must be analyzed. In our case, the problem is simplified, since, in the stationary case, the flow is potential, and the system of Eqs. (1) and (2) breaks up into two independent equations, which are solved in sequence. Examples of the velocity and pressure fields obtained for the TH 50/50 were presented in [15].

Experiments on Measuring the SAXS Signal

Small-angle scattering provides information on the distribution of electron density fluctuations in a sample. From the practical standpoint, this is an efficient tool for determining the characteristic particle size and the size distribution of particles in the object of investigation. The typical layout of an experiment aimed at measuring the SAXS is shown in Fig. 15. A spot 0.4–1.0 mm high and 3–20 mm wide is formed at the central part of the EM charge from the SR beam with the aid of upper K_1 and lower K_2 knives of the Kratki collimator. In front of the detector, the direct beam is shuttered by lower knife K_3. The deflected SAXS beams are detected by the detector. To perform additional monitoring, a fraction of the direct beam is passed through a filter (a copper plate 1 mm thick) and is incident on the detector.

The distance between knives K_1 and K_2 is ~200 mm. The distance between knife K_2 and the EM charge is ~700 mm; between the charge and knife K_3 ~ 640 mm; and between knife K_3 and the detector, ~ 260 mm. The angular range of SAXS measurements is $\sim 4 \times 10^{-4}$–10^{-2} rad. This measurement range allows detection of the SAXS from particles with a size of 1–100 nm.

The result of one of the experiments aimed at detecting the SAXS is shown in Fig. 16 [16]. The figure presents the spatial distribution of the SR photon flux obtained in a set of measurements, in which each next

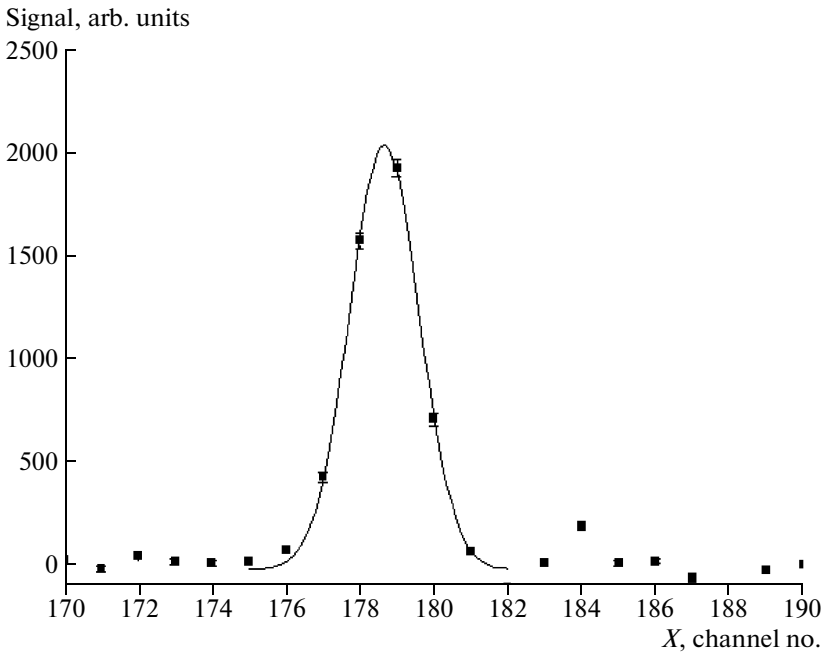

Fig. 10. Signal in the detector from a narrow beam; the FWHM corresponds to 2.1 channels.

measurement is taken 0.5 μs after the previous one. The measurement corresponding to an instant of 3.0 μs corresponds to passing of the detonation wave. It is apparent that formation of nanoparticles (nanodiamonds [16]) is initiated during the first μs after passing of the detonation wave and then increases in the next 4-μs interval. The mean size of nanoparticles in the sample can be calculated based on the shape of the SAXS distribution.

Possibilities of Use of the DIMEX Detector at the VEPP-4M

The DIMEX detector currently operates on the SR beam from the wiggler with a field of 2 T at the VEPP-3 with a beam energy of 2 GeV. The mean photon energy in the beam is ~20 keV after its passing through beryllium windows with a total thickness of 5 mm and a 1-cm-thick EM sample. Such a low energy makes it impossible to use thicker samples due

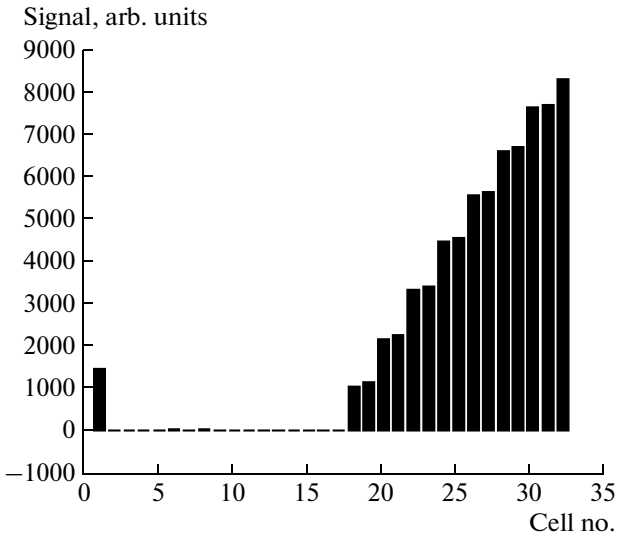

Fig. 11. Dependence of the signal on the number of the analog memory cell at a 125-ns measurement time interval without signal reset between measurements.

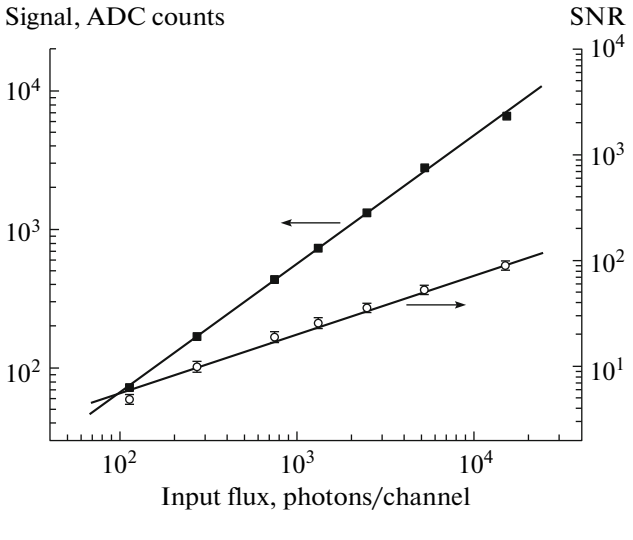

Fig. 12. Dependence of the signal in the detector and the SNR on the incident photon flux.

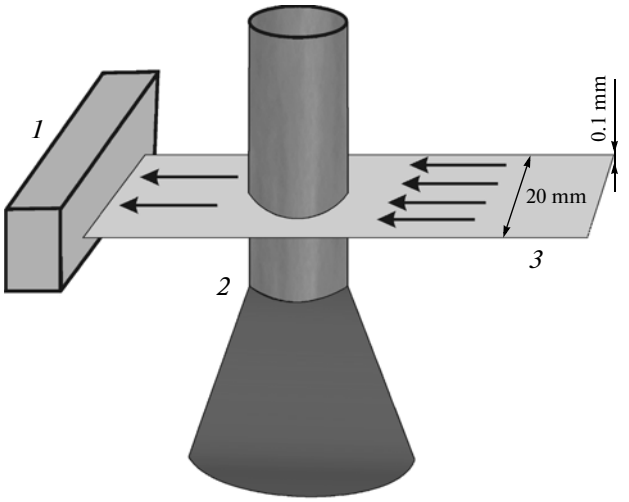

Fig. 13. Layout of the X-ray radiography experiment: (*1*) DIMEX detector, (*2*) EM charge under investigation, and (*3*) SR beam.

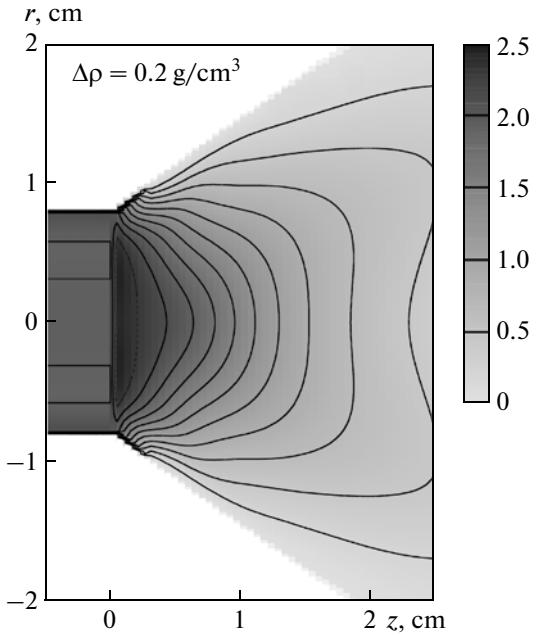

Fig. 14. Spatial density distribution ρ [g/cm] measured using the DIMEX detector; the charge was composed of trotyl and hexogen (TH 50/50).

to the significant absorption of the photon beam and, as a result, the limitation on the accuracy of material density measurements. A higher-energy beam can be obtained at the VEPP-4M storage ring with a 1.3-T wiggler, which is currently being designed. To estimate the detector parameters upon a change to the VEPP-4M beam, the experiment was simulated using the FLUKA2006.3 software package.

The expected energy spectrum of SR from the 5-pole wiggler with a field of 1.3 T at the VEPP-4M at a beam energy of 4 GeV is shown in Fig. 17. The figure presents the spectrum at the exit from the channel after passing through the beryllium windows with a total thickness of 5 mm and after passing through a 20-mm-thick EM sample. Carbon with a density of 1.2 g/cm^3 is the sample material. Hereinafter, this spectrum will be referred to as spectrum *3*. It is evident that the maximum of spectrum *3* is at an energy of 30 keV, and the spectrum density decreases twofold at an energy of ~50 keV and ≥10 times at an energy of 100 keV.

The fraction of the absorbed flux for spectrum *3* was determined by simulation. The detector model is composed of successive layers of carbon with a density of 1.2 g/cm^3 and a thickness of 1 mm, a 3-mm-thick layer of the Xe–CO_2 mixture (3 : 1) at a pressure of 7 atm, and a layer of the same mixture 30 mm thick and 1 mm high, in which the charge of absorbed photons is detected. A uniform photon flux with an energy distribution presented by spectrum *3* was incident on the model. The fraction of absorbed flux was determined as the ratio of photons absorbed in the 30-mm-thick working gas mixture to the incident photon flux. The value obtained is shown with dot *1* at an energy of 30 keV (the maximum in spectrum *3*) in Fig. 8.

The probability that a photon will be absorbed in the detector's sensitive volume fails to be the total characteristic of integrating detectors, among which the DIMEX detector can be ranked. This value ignores noise sources other than Poisson fluctuations of the absorbed flux, in particular, fluctuations of the absorbed photon energy. Detective quantum efficiency (*DQE*) [17–19] is a more complete characteristic of the detector:

$$DQE = \frac{SNR_{out}^2}{SNR_{in}^2}, \quad (3)$$

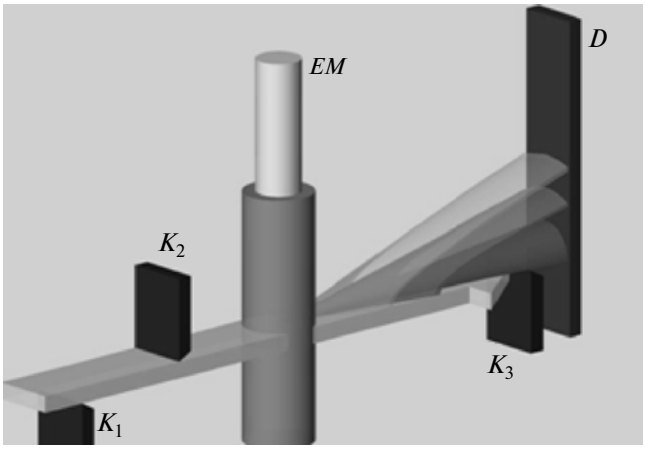

Fig. 15. Layout of the experiment aimed at detecting SAXS: (*EM*) cylindrical charge, (K_1) upper knife and (K_2, K_3) lower knives of the Kratki collimator, and (*D*) detector.

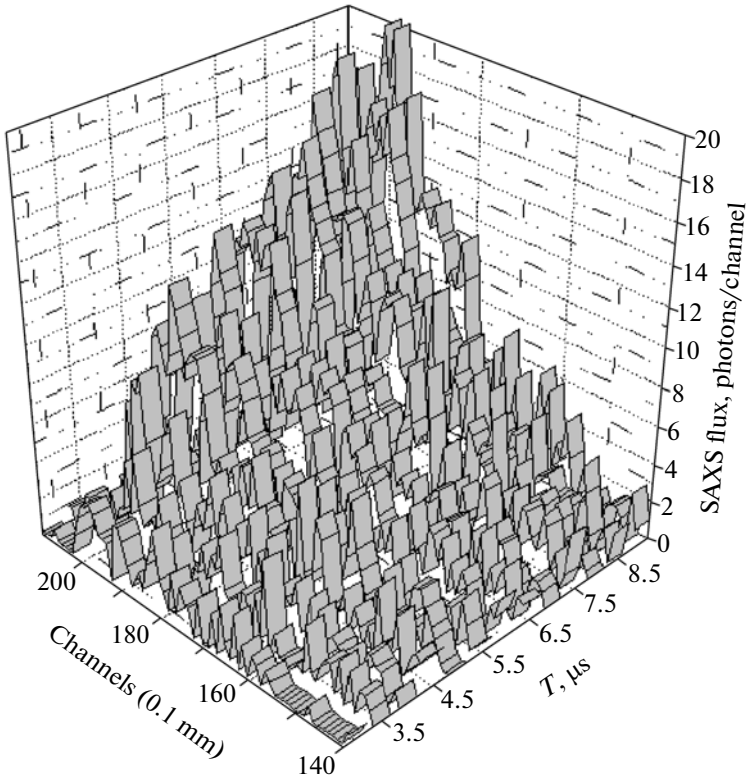

Fig. 16. Measured SAXS from the blasting sample.

where SNR_{out} is the SNR measured by the detector, and SNR_{in} is the SNR in the incident photon flux. For experimental measurement and simulation of the *DQE* value to be performed, the *DQE* must be expressed in terms of the measurable parameters. In this case, the generally accepted approach consists in presenting all characteristics in the spatial–frequency region, i.e., in terms of Fourier transforms of the spatial functions. If this representation is used, the characteristics of complex systems are divided into separate factors that can be analyzed independently of each other.

The Fourier transform of the output detector signal can be presented as $\bar{q}\,T(u)$, where $\bar{q}$ is the mean incident photon flux, and T is the characteristic function describing the transfer of the incident flux into the output signal versus spatial frequency u.

Therefore, the SNR at the detector output can be written in the form

$$SNR_{out}^2 = \frac{\left|\bar{q}T(u)\right|^2}{NPS(u)}, \tag{4}$$

where $NPS(u)$ is the noise power spectrum or the Fourier transform of the autocorrelation function

$$NPS(u) = F\{K(x)\}, \tag{5}$$

$$K(x) = \lim_{X\to\infty}\frac{1}{X}\int_X \Delta a(x')\Delta a(x'+x)dx'. \tag{6}$$

The input signal is equal to the mean photon flux $\bar{q}$, and the input noise is equal to the rms deviation of the input flux, i.e., $\sqrt{\bar{q}}$. Therefore,

$$SNR_{in}^2 = \bar{q}, \tag{7}$$

and

$$DQE(u) = \frac{q\left|T(u)\right|^2}{NPS(u)}. \tag{8}$$

The DQE value at zero spatial frequency is a convenient quantity, with which the detector can be characterized by a single number. At zero frequency, the noise power spectrum can be presented in the form

$$NPS(0) = \int_{-\infty}^{\infty} K(x)dx = X_{corr}K(0), \tag{9}$$

where X_{corr} is usually called the correlation length. The $K(0)$ value is the signal variance in the image σ^2; therefore,

$$NPS(0) = \sigma^2 X_{corr} \tag{10}$$

and

$$DQE(0) = \frac{\left|\bar{q}T(u)\right|^2}{\bar{q}X_{corr}\sigma^2} = \frac{SNR_{im}^2}{\bar{q}X_{corr}}, \tag{11}$$

where SNR_{im}^2 is the SNR in the image with the spatial noise correlations being ignored.

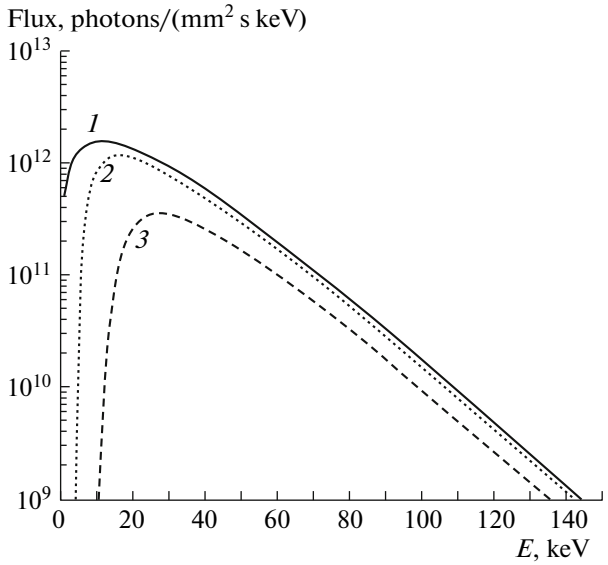

Fig. 17. SR spectra from the 5-pole wiggler with a field of 1.3 T at an electron energy of 4 GeV: (*1*) spectrum at the exit from the channel; (*2*) spectrum after passing though the beryllium windows at the exit from the channel, in the collimators module, and in the blasting chamber; and (*3*) spectrum after passing through the EM sample 20 mm thick.

As a result, the DQE can be calculated in terms of the parameters determined from the image recorded using the detector.

To calculate the DQE, we simulated the distribution of the energy deposited in the detector perpendicularly to the direction of strips in the readout structure, i.e., along the length of the entrance window. The uniform photon flux was incident on the detector in the 1-cm-long zone along the entrance window. The whole region was divided into 200 50-μm intervals. The mean value and the rms deviation of the energy deposited in these intervals were calculated. The SNR in the image was calculated as the ratio of the mean value to the rms deviation of the deposited energy. An infinitely thin photon beam was used to simulate the autocorrelation function, and the line spread function was obtained. The autocorrelation function coincides with the line spread function squared. The efficiency and the DQE obtained as a result of the simulation were 59 and 48%, respectively. The DQE is smaller than the photon absorption probability, since it takes into account fluctuations of the energy deposited upon absorption of a photon.

The simulation results obtained for the spatial resolution of the detector are shown in Figs. 18–21. The effect of the gas pressure on the spatial resolution is demonstrated in Fig. 18. Diffusion of electrons, which is inversely proportional to the square root of the pressure, is the key factor that governs the spatial resolution. Therefore, variations in the line spread function upon a change in the pressure from 7 to 10 atm are negligible. Further rising of the pressure is a complicated engineering problem, since it requires the appropriate increase in the high voltage applied to the detector electrodes (for the drift velocity of electrons to be maintained).

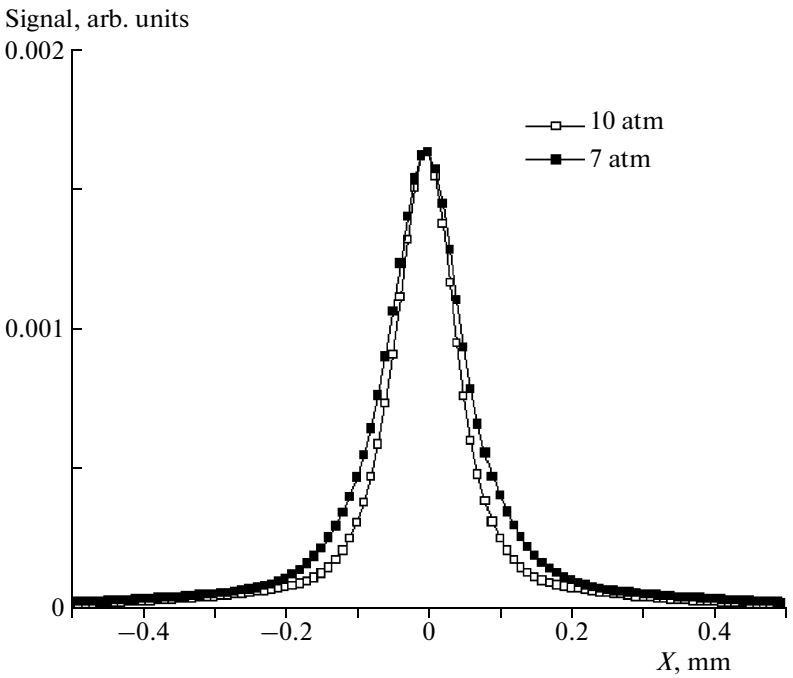

Fig. 18. Comparison of the line spread functions at 7- and 10-atm gas pressures in the detector; the photon energy was 50 keV.

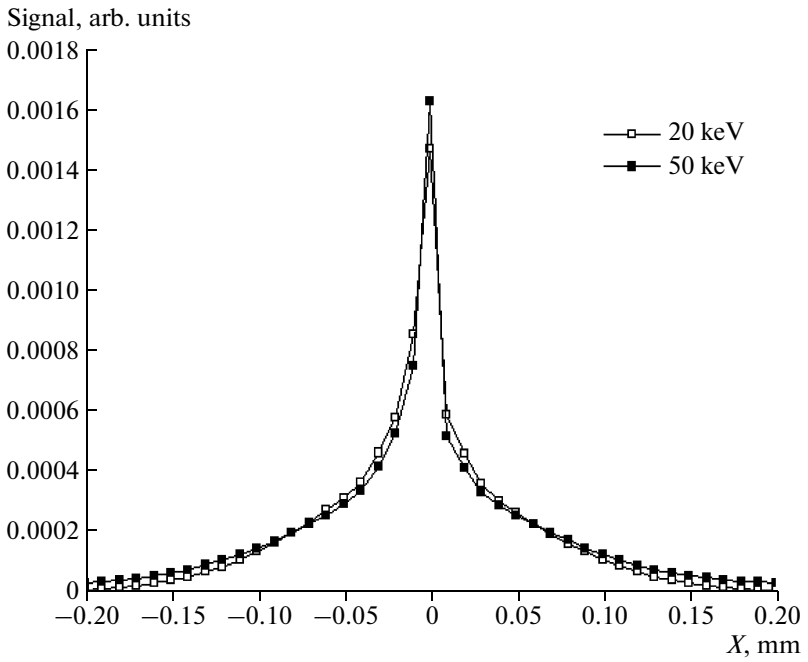

Fig. 19. Comparison of the line spread functions at energies of 20 and 50 keV with diffusion being ignored.

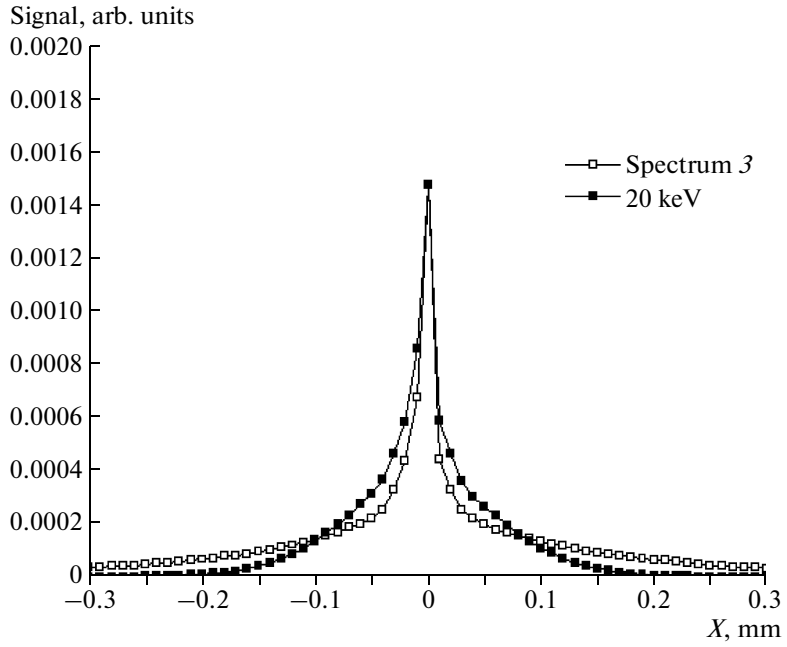

Fig. 20. Comparison of the line spread functions with diffusion being ignored for an energy of 20 keV and for the energy distribution corresponding to spectrum *3*.

Comparison of the line spread function for photon beams with different energies is presented in Fig. 19, in which the spatial resolutions for 20- and 50-keV photons (without diffusion) are compared. It is apparent that, in this energy range, the line spread function changes only slightly. In fact, the main contribution to the "smearing" of the line spread function is made by photoelectrons, the energy of which is ~15 keV at both values of the photon energy. The range of such an electron in the $Xe–CO_2$ mixture (3 : 1) at a pressure of 7 atm is ~100 μm on the average [20].

The spatial resolution for photons with the energy distribution corresponding to spectrum *3* is presented in Fig. 20. The line spread function for 20-keV pho-

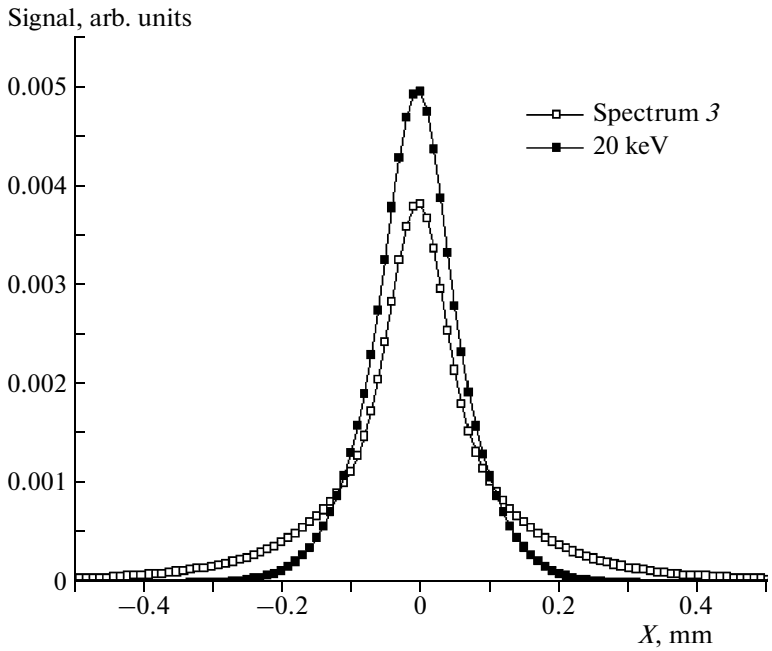

Fig. 21. Comparison of the spatial resolution for a photon energy of 20 keV and for the beam with the energy distribution corresponding to spectrum *3*.

tons is also presented in Fig. 20 for comparison. For better extraction of the effect from different photon energies, both line spread functions were calculated in the absence of diffusion. In Fig. 20, it is apparent that the line spread function for 20-keV photons is wider in its central part, which can be attributed to production of numerous low-energy photoelectrons from the beam with the distribution corresponding to spectrum *3*. In fact, as Fig. 17 shows, the spectral density in spectrum *3* slowly decreases at energies above the maximum (~30 keV), remaining rather high at energies above the *K*-edge energy of xenon (~35 keV). This results in production of many low-energy photoelectrons that have a very short range and provide high ionization density at the beam's point of incidence. On the other hand, the line spread function for spectrum *3* has long "tails," which can be attributed to the presence of high-energy photoelectrons both from the part of the spectrum at energies slightly lower than the xenon *K* edge, where photon absorption proceeds at the *L* edge, and from the high-energy part of the spectrum.

The total line spread function that takes into account the diffusion for the beam with the energy distribution corresponding to spectrum *3* is compared to the line spread function for 20-keV photons in Fig. 21. Both distributions are seen to have the same FWHM, although the distribution for spectrum *3* has more pronounced "tails." In both cases, the FWHM is close to 170 μm, which is in good agreement with the experimental result obtained at the VEPP-3 (Fig. 10).

A solid-state detector is considered to be an alternative for a gas-filled one. To study the properties of a possible alternative version, a silicon detector with a length of 1 cm along the beam and a thickness of 300 μm was simulated. The probability of Compton scattering (at least once), the probability of absorption (i.e., the photoeffect), and the total probability of a photon interacting in the detector material are shown in Fig. 22 versus the energy. Below 30 keV, the photon absorption probability is nearly unity, whereas the probability of Compton scattering is ~30% in the range of 20–100 keV. The figure also shows the photon interaction probability with the energy distribution corresponding to spectrum *3* and the DQE for this distribution.

Since Compton scattering results in deposition of energy by means of a recoil electron, this process was taken into account when calculating the efficiency. The average energy deposited in this process is substantially lower relative to photon absorption, which causes additional energy fluctuations and reduces the DQE. The efficiency (the interaction probability) for photons with the energy distribution according to spectrum *3* is ~81%, whereas the DQE is ~42%.

The spatial resolution of the silicon detector is substantially higher than that of the gas-filled DIMEX modification. The line spread function of the silicon detector, obtained by simulation for a photon beam with the energy distribution corresponding to spectrum *3*, is shown in Fig. 23. It is apparent that the FWHM of this distribution is ~20 μm.

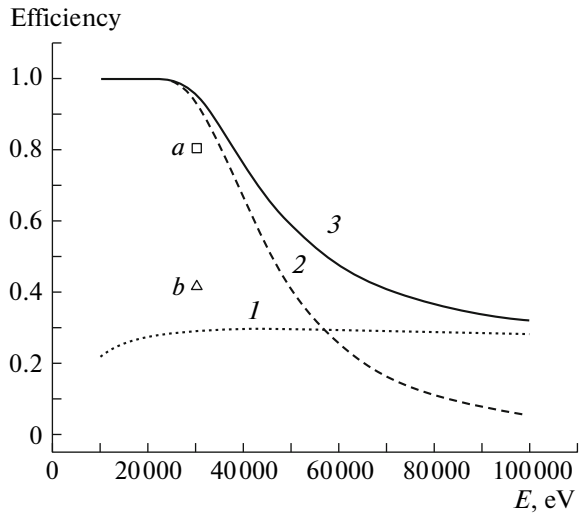

Fig. 22. Probability of photons interacting with the material of the silicon detector 1 cm in length and 0.3 mm in thickness: (*1*) probability of a single Compton scattering, (*2*) absorption (photoeffect) probability, (*3*) total interaction probability vs. energy, (*a*) simulation of the photon interaction probability and (*b*) DQE for the beam with the energy distribution corresponding to spectrum *3*.

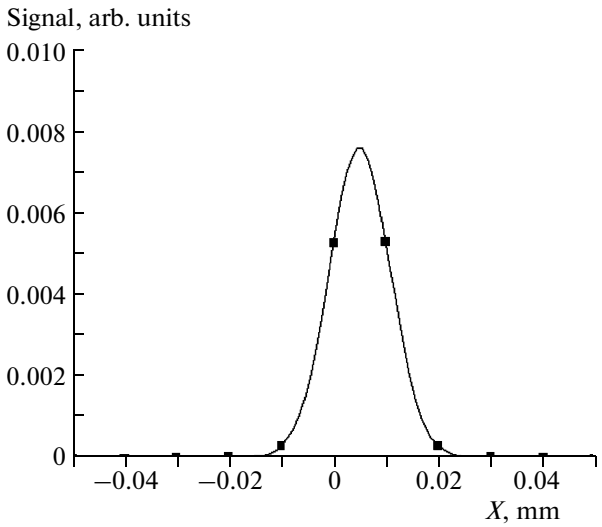

Fig. 23. Spatial resolution of the silicon detector for the SR beam with the energy distribution corresponding to spectrum *3*.

CONCLUSIONS

The experience gained over 6 years of operation of the DIMEX detector on the SR beamline at the VEPP-3 storage ring has demonstrated a considerable potential of the method for separate detection of radiation from individual bunches as applied to direct X-raying of a sample (X-ray radiography) and to measuring the SAXS. The available detector is capable of detecting SR with a mean energy of 20 keV, a spatial resolution of ~0.2 mm (FWHM), a maximum accuracy of ~1% (the maximum SNR is ~100), and a time resolution of $\leq 2.5 \times 10^{-4}$, which corresponds to the mixing coefficient for the signals from adjacent bunches.

In spite of the successful operation on the VEPP-3 beamline, it is desirable that the detector be further upgraded and that its characteristics be refined. Development of a wiggler with a field of 1.3 T for the VEPP-4M collider and building of the appropriate SR beamline will make it possible to increase the beam energy and intensity, which will offer a chance to conduct experiments with thicker samples. The simulation performed in our study shows that the detector will change its characteristics only slightly, its spatial resolution will remain ~0.2 mm, and its DQE will be ≈50%.

The spatial resolution and the maximum photon flux (the maximum SNR) detectable by the available detector are limited by the gas technology. These parameters can be substantially enhanced by using the solid-state technology. A silicon microstrip detector can be used in this technique if it is located at a small angle with the beam, so that the length on which the beam intersects the detector is ≥ 10 mm. In this case, the DQE will be rather high (~42%), whereas the spatial resolution of such a detector can be an order of magnitude better relative to the gas-filled DIMEX (~20 μm). Of course, this resolution can be attained only with appropriate segmentation of readout electrodes.

The experimental investigation of the properties of such a detector has already been started. It should be noted that this detector modification requires complete redesigning of the data acquisition electronics, as well as careful analysis of possible effects of radiation damage to the silicon under irradiation with an intense "white" SR beam.

REFERENCES

1. Aulchenko, V., Papushev, P., Ponomarev, S., et al., *J. Synchrotron Rad.*, 2003, vol. 10, p. 361.
2. Aulchenko, V., Ponomarev, S., Shekhtman, L., et al., *Nucl. Instrum. Methods Phys. Res. A*, 2003, vol. 513, p. 388.
3. Aulchenko, V.M., Evdokov, O.V., Shekhtman, L.I., et al., *J. Instr.,* 2008, vol. 3, p. 05005.
4. Sauli, F., *Nucl. Instrum. Methods Phys. Res. A*, 1997, vol. 386, p. 531.
5. Buzulutskov, A.F., *Prib. Tekh. Eksp.*, 2007, no. 3, p. 5 [*Instrum. Exp. Tech.* (Engl. Transl.), no. 3, p. 287].
6. Horisberger, R. and Pitzl, D., *Nucl. Instrum. Methods Phys. Res. A*, 1993, vol. 326, p. 92.
7. Fassó, A., Ferrari, A., Ranft, J., and Sala P.R., *CERN-2005-10, INFN/TC-05/11, SLAC-R-773.*
8. Fassó, A., Ferrari, A., Roesler, S., et al. *Computing in High Energy and Nucl. Phys. 2003 Conf. (CHEP2003)*, La Jolla, CA, USA, 2003; http://nicadd.niu.edu/~jer-

emy/lcd/doc/chep/03/SimAndModeling/MOMT005. PDF, eConf C0303241 (2003)MOMT005 [hep-ph/0306267].

9. Sharma, A. and Veenhof, R., http://consult.cern.ch/writeup/garfield/examples/gas/trans2000. html.
10. Bachmann, S., Bressan, A., Ropelewski, L., et al., *Nucl. Instrum. Methods Phys. Res., A* 1999, vol. 438, p. 376.
11. Pikalov, V.V. and Preobrazhenskii, N.G., *Rekonstruktivnaya tomografiya v gazodinamike i fizike plazmy* (Reconstruction Tomography in Gas Dynamics and Plasma Physics), Novosibirsk: Nauka SO, 1987.
12. Kozlovskii, V.N., *Informatsiya v impul'snoi rentgenografii* (Information in Pulsed X-ray Radiography), Snezhinsk, Russia: RFYaTs–VNIITF, 2006.
13. Pruuel, E.R., Merzhievskii, L.A., Ten, K.A., et al., *Fiz. Goreniya Vzryva*, 2007, vol. 43, no. 3, p. 121 [*Combustion, Explosion, and Shock Waves* (Engl. Transl.), no. 3, p. 355].
14. Evdokov, O.V., Kozyrev, A.N., Litvinenko, V.V., et al., *Nucl. Instrum. Methods. Phys. Res. A*, 2007, vol. 575, p. 116.
15. Ten, K.A., Pruuel, E.R., Merzhievsky, L.A., et al., *Nucl. Instrum. Methods Phys. Res. A*, 2009, vol. 603, p. 160.
16. Titov, V.M., Tolochko, B.P., Ten, K.A., et al., *Diam. Relat. Mater*, 2007, vol. 16, p. 2009.
17. Dainty, J.C. and Shaw, R., *Image Science: Principles, Analysis, and Evaluation of Photographic-Type Imaging Processes*, NJ.: Academic, 1974.
18. Beutel, J., Kundel, H.L., and Van Metter, R.L., *Handbook of Medical Imaging, vol. 1: Physics and Psychophysics*, SPIE Press, 2000.
19. Porosev, V.V., Shekhtman, L.I., Zelikman, M.I., and Blinov, N.N., Jr., *Meditsinskaya Tekhnika*, 2004, no. 5, p. 16.
20. Tabata, T., Ito, R., Okabe, S., et al., *Nucl. Instrum. Methods Phys. Res.*, 1972, vol. 103, p. 85.